Journal of
Materials Chemistry A

PAPER

View Article Online
View Journal | View Issue

Cite this: *J. Mater. Chem. A*, 2016, **4**, 5647

Achieving high-performance planar perovskite solar cell with Nb-doped TiO₂ compact layer by enhanced electron injection and efficient charge extraction†

Bai-Xue Chen, Hua-Shang Rao, Wen-Guang Li, Yang-Fan Xu, Hong-Yan Chen, Dai-Bin Kuang* and Cheng-Yong Su

Received 1st February 2016
Accepted 4th March 2016

DOI: 10.1039/c6ta00989a

www.rsc.org/MaterialsA

The power conversion efficiency (PCE) of a planar perovskite solar cell (PSC) is closely associated with the conduction band energy, conductivity and coverage of the compact layer. However, as the most widely used compact layer material, TiO_2 has unfavorable electrical properties such as low electron mobility and conductivity; as a result, modifications such as elemental doping are of paramount importance. In this study, Nb-doped TiO_2 with improved carrier density and conductivity was prepared *via* a facile one-pot solution process and applied successfully as a high-quality compact layer for planar PSCs. A positive shift in the flat-band potential (V_{fb}) and increased conductivity after Nb doping efficiently facilitated photogenerated electron injection and charge extraction from the perovskite film to the 2% Nb-doped TiO_2 compact layer, contributing to impressive advances in photovoltaic performance compared with pristine TiO_2. Ultimately, a PSC assembled using optimized 2% Nb-doped TiO_2 and $CH_3NH_3PbI_3$ yielded a power conversion efficiency of up to 16.3%.

Introduction

In the past few years, organic–inorganic hybrid perovskites have shown striking potential in applications of photovoltaic cells,[1–3] sensors,[4] light-emitting diodes,[5] lasers,[6] and photodetectors.[7] In the field of organometal trihalide perovskite solar cells, breakthroughs and progress have already been witnessed owing to the intriguing photoactive properties of $CH_3NH_3PbX_3$ (X = Cl, Br, I) such as a wide absorption range,[8] high extinction coefficient,[9] and long electron–hole diffusion length.[10] Currently, the efficiencies of PSC devices are still constantly increasing,[11] one of which has already risen to the incredible rate of 21.0%.[12]

In general, PSCs have three main types of device architecture: (1) mesoscopic structures using mesoporous semiconducting materials as electron transport layers (ETLs) (*e.g.* TiO_2,[13] WO_3,[14] $SrTiO_3$,[15] ZnO,[16] Zn_2SnO_4 (ref. 17) and SnO_2 (ref. 18)), (2) meso-superstructures employing mesoporous insulators such as Al_2O_3 (ref. 19) and ZrO_2 (ref. 20) as scaffolds while perovskite itself acts as an ETL, and (3) planar structures using ultra-thin compact layer materials (*e.g.* TiO_2,[21] modified TiO_2,[4,22] ZnO,[23] SnO_2 (ref. 24 and 25) and WO_3 (ref. 26)) for both hole-blocking and electron-conducting purposes. Among these types, planar PSCs are preferred for reasons of a simpler process and lower cost for future applications. In planar PSC devices, the compact layer extracts and transports photogenerated electrons from the perovskite absorber to the FTO (F: SnO_2) glass substrate and prevents contact between the FTO and the hole transport layer (HTM). Therefore, high-quality film, appropriate conduction band, and superior electron mobility and conductivity of the compact layer material are responsible for high efficiency in planar PSC devices by reducing excessive charge accumulation and guaranteeing effective electron injection at the compact layer/perovskite interface, which can be achieved by modification of TiO_2 such as doping. For instance, Y-doped TiO_2 (ref. 4) was utilized as an effective compact layer in a planar PSC device with a high PCE of 19.3% (without a mask). Niobium-doped TiO_2, which has been used as a potential transparent conducting oxide (TCO)[27,28] and dye-sensitized solar cell (DSSC)[29,30] photoanode, has proved its ability to accelerate electron extraction as an electron mediator in PSCs.[31] Niobium-doped TiO_2 for mesoscopic PSC[32,33] applications has not achieved satisfying PCEs so far; the highest efficiency has been 13.4%. Furthermore, devices assembled using a Nb-doped TiO_2 compact layer and mesoporous TiO_2 film merely attained a maximum PCE of 10.26%,[34] which was possibly due to the quality of the compact layer and perovskite material.

Here, for the first time, a homogeneous Nb-doped TiO_2 nanocolloidal solution was developed to form a high-quality

---

MOE Key Laboratory of Bioinorganic and Synthetic Chemistry, Lehn Institute of Functional Materials, School of Chemistry and Chemical Engineering, Sun Yat-sen University, Guangzhou 510275, P. R. China. E-mail: kuangdb@mail.sysu.edu.cn; Fax: +86-20-8411-3015

† Electronic supplementary information (ESI) available. See DOI: 10.1039/c6ta00989a

compact layer for efficient perovskite solar devices. Nb doping led to a positive shift in V_{fb} and a conspicuous improvement in conductivity compared with pristine TiO_2. Thus, as expected, electron injection and extraction were substantially enhanced and a significant improvement in PCE (from 14.9% to 16.3%) was witnessed with the optimized 2% Nb doping. Further characterization, such as Mott–Schottky analysis, photoluminescence (PL) spectra, time-resolved photoluminescence (TRPL) spectra, and electrochemical impedance spectra (EIS), was also carried out to reveal the mechanism behind the enhancement caused by Nb doping.

Experimental

Synthesis of TiO_2 and Nb-doped TiO_2 colloidal solution precursors

A Nb-doped TiO_2 colloidal solution was prepared according to a modification of the method used for a pristine TiO_2 colloidal solution in our previous reports.[35–37] First, the correct amount of niobium chloride (0.284 mmol, 0.568 mmol, 0.852 mmol, and 1.42 mmol) was added to 10 mL titanium butoxide in different molar ratios (1%, 2%, 3%, and 5%). The dissolution process lasted for a few minutes in a sonication bath until a homogeneous solution was formed. Following that, the uniform solution was added dropwise with stirring to a flask containing acetylacetone (3.41 mL), *n*-butanol (12.54 mL), *para*-toluenesulfonic acid (1.27 g) and deionized water before being refluxed at 60 °C for 12 h. A TiO_2 colloidal solution was obtained by a similar approach but excluding the addition of niobium chloride.

Synthesis of CH_3NH_3I

CH_3NH_3I was synthesized by blending methylamine (33 wt% in methanol) and hydroiodic acid (57 wt% aqueous) in a molar ratio of 1.5 : 1 in an ice-water bath with stirring for 2 h, then crystallized by rotary evaporation and purified by recrystallization from diethyl ether before being dried in a vacuum and stored in a N_2 atmosphere.

Fabrication of perovskite solar cells

FTO glass (8 Ω square^{-1}) was pretreated with 4 M HCl and zinc powder. The etched substrates were then cleaned with deionized water, alcohol and acetone *via* an ultrasonic process. The Nb-doped TiO_2 compact layer was formed by spin-coating the obtained colloidal solution diluted threefold in anhydrous ethanol at 2000 rpm for 60 s, followed by annealing at 500 °C for 1 h in ambient air. A similar approach was used for the pristine TiO_2 compact layer. The annealed TiO_2 and Nb-doped TiO_2 compact layers were immersed in a 0.04 M aqueous solution of $TiCl_4$ at 70 °C for 30 minutes before being sintered at 520 °C for 30 minutes. The fabrication of the $CH_3NH_3PbI_3$ perovskite layer on the compact layer was carried out by spin-coating a precursor solution containing 0.88 M $PbCl_2$ and 2.64 M CH_3NH_3I dissolved in DMF at 5000 rpm for 60 s and annealing at 95 °C for 2 h. An HTM solution comprising 73.2 mg mL^{-1} spiro-OMeTAD (2,2′,7,7′-tetrakis-(*N*,*N*-di-*p*-methoxyphenyl-amino)-9,9′-spirobifluorene)/chlorobenzene with the addition of 28.8 μL 4-*tert*-butylpyridine (*t*-BP) and 17.5 μL bis(trifluoromethane)sulfonimide lithium salt (Li-TFSi) solution (520 mg in acetonitrile) was then deposited by spin-coating at 5000 rpm for 60 s. Finally, the metal electrode was deposited by magnetron sputtering of gold.

Characterization

The phase structure was characterized using a Bruker D8 Advance X-ray diffractometer (Cu Kα radiation, $\lambda = 1.5418$ Å). X-ray photoelectron spectroscopy (XPS) was carried out using a photoelectron spectrometer (ESCALAB 250Xi, Thermo Fisher Scientific). Field emission scanning electron microscopy and energy-dispersive spectroscopy (FE-SEM and EDS, JSM-6330F) were utilized to investigate the morphology of PSC devices and the amount of niobium dopants. The morphologies of the surfaces of pristine TiO_2 and 2% Nb-doped TiO_2 deposited on FTO glass substrates were characterized by atomic force microscopy (AFM, Dimension FastScan). Mott–Schottky plots were obtained using an electrochemical workstation (Zahner Zennium) in a standard three-electrode configuration with Ag/AgCl (in saturated KCl) as the reference electrode and Pt mesh as the counter electrode in 0.1 M NaCl electrolyte. The frequency was 80 mHz, whereas the amplitude potential was 10 mV. The photovoltaic performance of PSCs was recorded using a Keithley 2400 source meter with a delay time of 100 ms under one-sun AM 1.5G (100 mW cm^{-2}) illumination with a solar light simulator (Oriel, Model: 91192), which was calibrated using a NREL standard Si solar cell. The active areas of all solar cells were defined by a 12.56 mm^2 metal mask. Incident photon-to-current conversion efficiency (IPCE) spectra were obtained on a Keithley 2000 multimeter as a function of the wavelength from 380 to 850 nm on the basis of a Spectral Products DK240 monochromator. Photoluminescence (PL) (excitation at 406.2 nm) and time-resolved photoluminescence (TRPL) (excitation at 406.2 nm and emission at 760 nm) spectra were obtained with an Edinburgh Instruments Ltd FLSP920 spectrometer. EIS spectra were also acquired using the electrochemical workstation in the frequency range from 100 mHz to 4 MHz, applying the open-circuit voltage derived from the *J*–*V* test and under illumination conditions of 100 mW cm^{-2} (AM 1.5G).

Results and discussion

Characterization of Nb-doped TiO_2

The X-ray diffraction (XRD) patterns of pristine TiO_2 and Nb-doped TiO_2 with different Nb contents are shown in Fig. 1a and b. It is obvious that the anatase phase is retained in all the samples irrespective of the increase in niobium concentration, whereas the (101) anatase peaks are shifted towards lower values of 2θ (Fig. 1b), which is ascribed to the ionic radius of Nb^{5+} (0.64 Å) being larger than that of Ti^{4+} (0.61 Å), according to the Bragg equation $2d \sin \theta = \lambda$.[30] The XPS survey spectrum (Fig. S1†) demonstrates the presence of Nb in 2% Nb-doped TiO_2 film. The XPS spectra of pristine TiO_2 and 2% Nb-doped TiO_2 (Fig. 1c) clearly show that the Ti^{4+} states with a binding

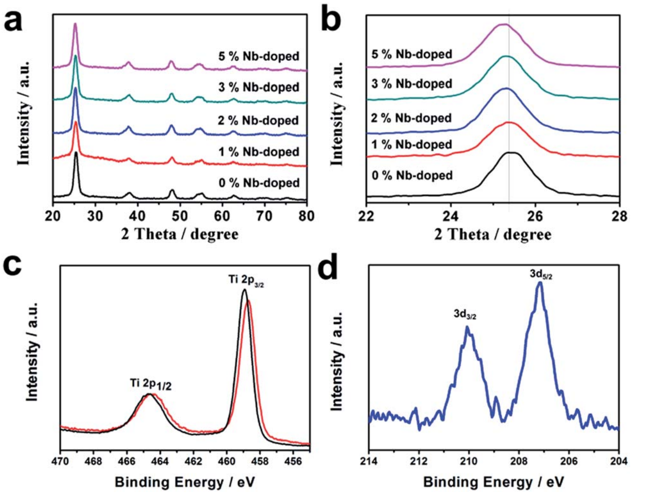

Fig. 1 (a) XRD patterns of pristine TiO_2 and Nb-doped TiO_2 films with different amounts of Nb. (b) Details of the XRD patterns for the (101) plane. (c) XPS spectra of Ti^{4+} states of pristine TiO_2 and 2% Nb-doped TiO_2 and (d) Nb^{5+} states found in 2% Nb-doped TiO_2.

energy (BE) of 459.1 eV (pristine TiO_2) for the Ti $2p_{3/2}$ peak are shifted to 458.9 eV upon Nb doping. Moreover, the Nb^{5+} state with a BE of 207.2 eV for the $3d_{5/2}$ transition is also confirmed, as shown in Fig. 1d. Quantitative analysis of the Nb concentration was performed *via* energy-dispersive X-ray spectroscopy (EDX), of which the results (Fig. S2†) are in agreement with the theoretical values.

To investigate the changes in electrical properties caused by the introduction of niobium, Mott–Schottky analyses[38] and current–voltage (I–V) measurements[39] were carried out, the results of which are shown in Fig. 2. The carrier density (N_d) can be calculated by fitting a Mott–Schottky plot (Fig. 2a) according to eqn (1) as follows:

$$N_d = -(2/e\varepsilon_0\varepsilon)(d(1/C^2)/dV)^{-1} \tag{1}$$

where ε_0 is the permittivity of a vacuum (8.85×10^{-12} F m^{-1}), ε is the dielectric constant of anatase (55 F m^{-1}),[40] and e is the elementary charge. As a result, the obtained values of N_d are displayed in Table 1. It is concluded that the carrier density increases with an increase in the Nb content.

Table 1 Carrier density and conductivity of pristine TiO_2 and Nb-doped TiO_2 films with different Nb concentrations

	N_d/cm^{-3}	σ_0/mS cm^{-1}
Pristine TiO_2	3.0×10^{19}	1.74×10^{-3}
1% Nb-doped TiO_2	3.9×10^{19}	4.8×10^{-3}
2% Nb-doped TiO_2	4.8×10^{19}	8.0×10^{-3}
3% Nb-doped TiO_2	5.2×10^{19}	1.15×10^{-2}
5% Nb-doped TiO_2	6.0×10^{19}	1.28×10^{-2}

To determine the direct-current conductivity (σ_0)[41] of various Nb-doped TiO_2 materials, devices composed of ITO/Nb-doped TiO_2/Au were fabricated and the current–voltage (I–V) characteristics are shown in Fig. 2b. From eqn (2),

$$I = \sigma_0 A D^{-1} V \tag{2}$$

where A is the area (16 mm^2) and D is the thickness (100 nm) of the sample; the calculated values of the direct-current conductivity are summarized in Table 1 and exhibit approximately the same trend as the changes in N_d with different Nb concentrations.

In other words, both N_d and σ_0 increase with an increase in the Nb dopant concentration.

Structure of perovskite solar cell device

Fig. 3a shows a cross-sectional scanning electron microscopy (SEM) image of a sandwich-like planar PSC device with thicknesses of the compact layer (2% Nb-doped TiO_2), perovskite ($CH_3NH_3PbI_3$), HTM (spiro-OMeTAD), and Au cathode of approximately 80 nm, 250 nm, 150 nm, and 80 nm, respectively. Fig. 3b and S3† present top-view SEM images of perovskite layers deposited on Nb-doped TiO_2 compact layers with various dopant contents from 0% to 5%. In comparison with an SEM image of perovskite deposited on pristine TiO_2 (ESI, Fig. S3a†), it is obvious that even though the pristine TiO_2 and 2% Nb-doped TiO_2 compact layers have similar roughnesses (ESI, Fig. S4†), perovskite deposited on the 2% Nb-doped TiO_2 layer has fewer pinholes. The XRD pattern of perovskite deposited on FTO glass is shown in Fig. S5.† The four characteristic peaks identified at 14.5°, 28.5°, 43.2°, and 58.8° are assigned to the (110), (220), (330), and (440) planes of the $CH_3NH_3PbI_3$ phase, whereas the other four characteristic peaks marked with star symbols are indexed to the (110), (101), (200), and (211) planes of FTO.

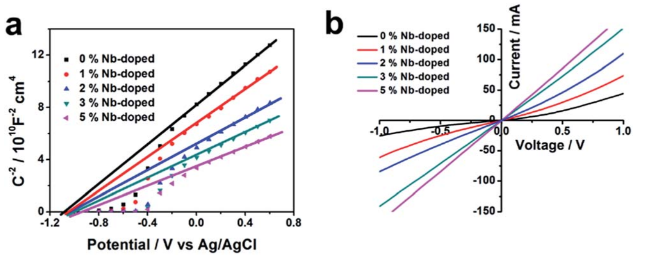

Fig. 2 (a) Mott–Schottky plots of pristine TiO_2 and Nb-doped TiO_2 films with different amounts of Nb. (b) I–V characteristics of ITO/TiO_2/Au and ITO/Nb-doped TiO_2 with different Nb contents/Au device.

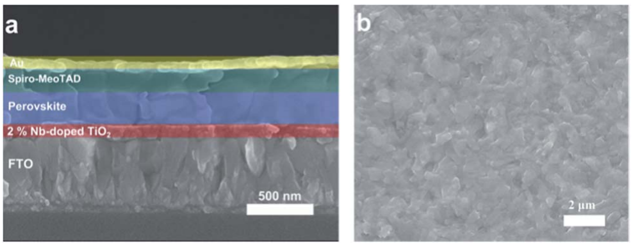

Fig. 3 (a) Color-enhanced cross-sectional SEM micrograph of typical PSC based on 2% Nb-doped TiO_2 and (b) top-view SEM image of $CH_3NH_3PbI_3$ deposited on 2% Nb-doped TiO_2 compact layer.

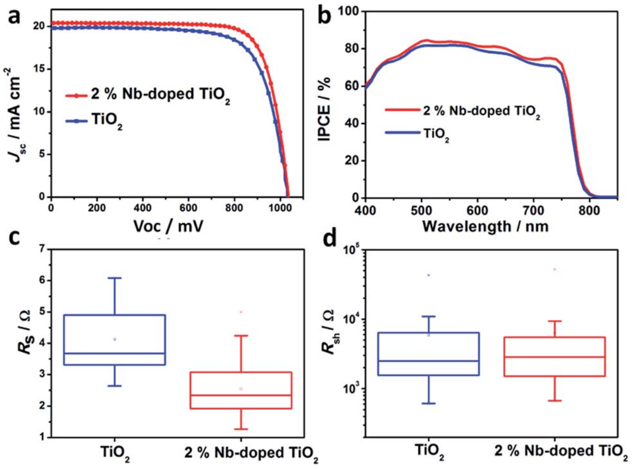

Fig. 4 (a) J–V curves of champion perovskite solar cells based on 2% Nb-doped TiO_2 and TiO_2 compact layers measured under AM 1.5G one-sun (100 mW cm^{-2}) illumination. (b) Incident photon-to-current conversion efficiency (IPCE) of champion perovskite solar cells. (c) Values of R_s and (d) R_{sh} for PSCs based on pristine TiO_2 and 2% Nb-doped TiO_2, respectively.

Photovoltaic performance of PSC

The average photovoltaic performance parameters of PSC devices based on Nb-doped TiO_2 with various dopant contents are shown in Fig. S6.† There is a pronounced increase in J_{sc} for PSCs based on Nb-doped TiO_2 compact layers from 18.8 mA cm^{-2} (pristine TiO_2) to 20.8 mA cm^{-2} (5%), which can be attributed to the increased carrier density and conductivity upon Nb doping. Nevertheless, the coverage of perovskite deposited on the compact layer is regarded as another factor that influences the entire photovoltaic performance of PSCs. According to the variation in the number of pinholes in Nb-doped TiO_2 films at different dopant contents (shown in Fig. 3b and S3†), the coverage of perovskite substantially increased from 0% to 2% Nb content, remained nearly the same at 3%, but significantly decreased from 3% to 5%. These findings indicate the variation in FF values from 0% to 5% Nb content. Eventually, 2% Nb-doped TiO_2 was selected as an ideal compact layer for planar PSC devices.

Fig. 4a shows the current density–voltage (J–V) characteristics of the best-performing PSC devices based on pristine TiO_2 and 2% Nb-doped TiO_2 compact layers, of which the derived performance parameters are shown in Table 2. Thus, the PSC based on 2% Nb-doped TiO_2 has an average short-circuit photocurrent density of 20.0 mA cm^{-2}, an open-circuit voltage of 999 mV and a fill factor of 0.76, yielding an average efficiency of 15.3%, whereas the PCE of the best-performing device is 16.3%. In the same batch, the PSC based on pristine TiO_2 has an average short-circuit photocurrent density of 18.8 mA cm^{-2}, an open-circuit voltage of 987 mV and a fill factor of 0.71, yielding an average PCE of 13.3%, whereas the PCE of the champion cell is 14.9%. It is apparent that the significant increase in PCE relies more on increases in the short-circuit current density and fill factor upon doping with 2% Nb, in contrast to pristine TiO_2. Such a variation in J_{sc} is likely to stem from two effects caused by doping with niobium cations. One is the improvement in the electron injection efficiency resulting from the positive shift in V_{fb} upon Nb doping, as shown in the Mott–Schottky plots (Fig. 2a). The other is the increased charge transfer ability due to the increases in carrier density and electron conductivity for 2% Nb-doped TiO_2, as displayed in Table 1.

The incident photon-to-electron conversion efficiency (IPCE) or external quantum efficiency of the planar perovskite solar cells based on TiO_2 and 2% Nb-doped TiO_2 compact layers are shown in Fig. 4b, which exhibits an obvious onset of the generation of photocurrent at 780 nm, in accordance with the band gap of $CH_3NH_3PbI_3$. The corresponding results have revealed high IPCE values along the entire range of wavelengths from 400 nm to 780 nm at 2% Nb content. The integrated current densities from IPCE spectra for TiO_2 and 2% Nb-doped TiO_2 are 18.4 mA cm^{-2} and 19.2 mA cm^{-2}, which are in reasonable agreement with the measured values of J_{sc}.

To explain the variations in fill factor, the series resistance (R_s) and shunt resistance (R_{sh}) were derived from the J–V curves, as shown in Fig. 4c and d. It is notable that devices based on a 2% Nb-doped TiO_2 ETL have lower values of R_s, which is consistent with the higher FF. Moreover, the R_{sh} values of these two types of cells are of the same order of magnitude, but a little higher for 2% Nb-doped TiO_2. Hence, it is concluded that the Nb-doped TiO_2 layer functions well as an electron-transporting layer and a hole-blocking layer owing to its increased carrier density, enhanced electron conductivity and dense morphology.

Both forward and reverse-bias sweeps were used to determine the hysteresis behaviour of PSCs.[42] The hysteresis behaviour is possibly caused by ion migration,[43] ferroelectricity,[44] and imbalances in charge transportation or extraction.[39] According

Table 2 Maximum PCE and average values of photovoltaic parameters for 30 devices derived from recording current density–voltage curves under simulated one-sun illumination (100 mW cm^{-2}, AM 1.5)

		J_{sc}/mA cm^{-2}	V_{oc}/mV	PCE/%	FF	$R_s{}^a$/Ω	$R_{sh}{}^b$/Ω
TiO_2	Average	18.8	987	13.3	0.71	4.1	5901.8
	Max	19.8	1032	14.9	0.73	4.7	6394.7
2% Nb-doped TiO_2	Average	20.0	999	15.3	0.76	2.5	6258.4
	Max	20.4	1036	16.3	0.77	2.4	4051.8

[a] R_s values in the 'Max' rows are those of the device with the maximum PCE. [b] R_{sh} values in the 'Max' rows are those of the device with the maximum PCE.

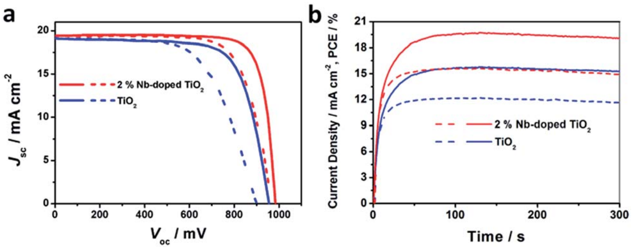

Fig. 5 (a) *J*–*V* curves recorded from forward bias to short circuit (FB-SC, solid lines) and from short circuit to forward bias (SC-FB, dashed lines) at a delay time of 100 ms for the typical PSC devices based on both 2% Nb-doped TiO_2 and pristine TiO_2. (b) Steady-state current (solid lines) measured at forward bias and stabilized power output (dashed lines) under simulated AM 1.5G sunlight of 100 mW cm^{-2}.

to the *J*–*V* curves (Fig. 5a) recorded from forward bias to short circuit (FB-SC) and from short circuit to forward bias (SC-FB), as well as the specific photovoltaic parameters (Table S1†) of typical perovskite solar cells based on different compact layers, the PCE for SC-FB is 90.0% of that for FB-SC for the device based on 2% Nb-doped TiO_2, but only 81% for that based on pristine TiO_2. This result is ascribed to the enhanced charge extraction at the compact layer/perovskite interface as a result of niobium doping. Owing to the efficient charge extraction, the accumulation of charge at the interface was substantially reduced, finally resulting in the reduction in hysteresis of the device based on 2% Nb-doped TiO_2.

Stabilized power output under applied bias at the maximum power point is deemed to be another significant parameter that reflects the real sustainable power conversion efficiency of solar cells.[45,46] Here, by subjecting the best-performing device based on 2% Nb-doped TiO_2 to measurements of steady-state current and maximum power output at a forward bias of 800 mV under simulated AM 1.5G sunlight of 100 mW cm^{-2}, a maximum PCE of 15.8% (shown in Fig. 4b) was obtained. However, in the same batch, the device based on pristine TiO_2 merely yielded a maximum PCE of 12.0% at a forward bias of 760 mV.

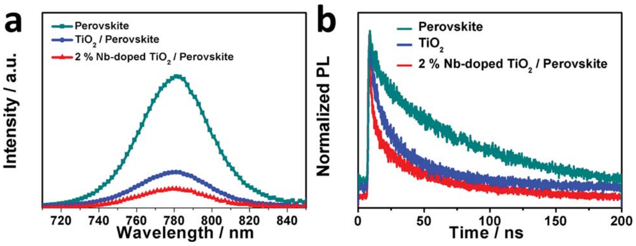

Fig. 6 (a) Photoluminescence (PL) spectra (excitation at 406.2 nm) and (b) time-resolved photoluminescence (TRPL) spectra (excitation at 406.2 nm and emission at 760 nm) of bare perovskite film and perovskite film on pristine TiO_2 and 2% Nb-doped TiO_2.

Recombination process of PSCs

Photoluminescence (PL) and time-resolved photoluminescence (TRPL) measurements were carried out to determine whether or not the photogenerated electrons were efficiently injected from the perovskite film into the compact layer.[47–49] Fig. 6a shows the steady-state PL spectra of perovskite, TiO_2/perovskite and 2% Nb-doped TiO_2/perovskite deposited on a blank glass. From the intensity of the photoluminescence peak at 780 nm, the $CH_3NH_3PbI_3$ perovskite film deposited on 2% Nb-doped TiO_2 shows more evident PL quenching compared with pristine TiO_2 film, which proves that Nb doping has successfully increased the rate of carrier extraction at the compact layer/perovskite interface. Furthermore, time constants τ_e were obtained by fitting TRPL curves (Fig. 6b) to determine the exciton lifetime of perovskite on different electrodes. As a result, the fitted time constants τ_e of perovskite film, TiO_2/perovskite and 2% Nb-doped TiO_2/perovskite are calculated to be 18.7, 2.42 and 1.96 ns, respectively. Thus, compared with pristine TiO_2, the PL decay of 2% Nb-doped TiO_2 is approximately 19% faster, which indicates that the time needed for electron injection from perovskite film into 2% Nb-doped TiO_2 is shorter than that into pristine TiO_2. The enhanced electron injection, which is possibly ascribed to the positive shift in V_{fb} upon Nb doping, contributes to more efficient extraction of photogenerated carriers at the compact layer/perovskite interface, resulting in the increased PCE.

EIS measurements were also carried out to acquire a better understanding of the interfacial charge transport processes and recombination dynamics of PSC devices based on pristine TiO_2 and 2% Nb-doped TiO_2. Fig. S7† displays Nyquist plots for these two cells measured at their own open-circuit potential under one-sun AM 1.5G illumination. According to the Nyquist plots, two distinct RC arcs are observed; the small semicircle in the high-frequency range (left) is assigned to hole diffusion in the HTM layer, whereas the large semicircle at low frequency (right) is attributed to the recombination process.[50–52] A traditional simplest equivalent circuit (shown inside Fig. S7†) is used to fit the data in the Nyquist plots. The fitted values of R_{series} and the recombination resistance (R_{rec}) are tabulated in Table S2.† The values of R_{series} of the devices based on TiO_2 and 2% Nb-doped TiO_2 compact layers measured by EIS are 17.8 and 8.7 Ω cm^2, respectively. Because the FTO layer, perovskite film, HTM layer and Au film of both devices were fabricated in the same process, the decrease in R_{series} is primarily attributed to the increased conductivity upon doping with 2% Nb. This decreased value of R_{series} for 2% Nb-doped TiO_2 contributes to the increase in the FF compared with that of pristine TiO_2. In addition, the calculated values of R_{rec} for PSCs based on TiO_2 and 2% Nb-doped TiO_2 films are 610.1 and 691.5 Ω cm^2, respectively, which indicates a reduction in recombination for the latter owing to the increased charge transfer rate. These findings can be ascribed to the positive shift in the conduction band, which reduces energy loss and facilitates the injection of photogenerated electrons. Because the open-circuit voltage of a planar perovskite solar device has been discovered to rely more on perovskite itself rather than the conduction band energy of the metal oxide compact layer,[53,54] it is reasonable that devices based on 2% Nb-doped TiO_2 should achieve a higher open-circuit voltage as a result of reduced recombination, regardless of the small variation in potential difference between the quasi-Fermi level of the compact layer and the HTM, which is slightly different from DSSCs. In conclusion, niobium doping leads to an increase in film conductivity and a reduction in recombination resistance, which contribute to substantial increases in FF, J_{sc} and V_{oc}.

Conclusions

In summary, a simple, low-cost, homogeneous Nb-doped TiO_2 nanocolloidal solution has been developed for forming a high-quality compact layer for efficient perovskite solar devices. Upon optimization of the Nb dopant content, the optimal 2% Nb-doped TiO_2 compact layer has demonstrated a PCE of as high as 16.3% ($J_{sc} = 20.4$ mA cm^{-2}, $V_{oc} = 1036$ mV, and FF $= 0.77$) measured with a stabilized maximum power output at an efficiency of 15.8%, which is a record for PSCs based on a Nb-doped TiO_2 compact layer at present. Niobium doping leads to impressive increases in carrier density and film conductivity and a positive shift in V_{fb}. Such improvements lend crucial support to the enhanced injection and extraction of photogenerated electrons at the compact layer/perovskite interface, which sequentially trigger remarkable increases in J_{sc} and FF. Niobium doping also contributes to enhanced PL quenching and a faster PL decay time owing to the improved extraction of photogenerated electrons. In general, the fabrication and optimization of Nb-doped TiO_2 offer significant potential in the search for alternative compact layers that possess matching band gaps and enhanced conductivity with prospects for high-performance PSC devices.

Acknowledgements

The authors acknowledge financial support from the National Natural Science Foundation of China (91433109, 91222201), the Program of Guangzhou Science and Technology (201504010031), the Fundamental Research Funds for the Central Universities, the State Key Laboratory of Optoelectronic Materials and Technologies (Sun Yat-sen University) and the NSF of Guangdong Province (S2013030013474, 2014A030313148).

Notes and references

1 A. Kojima, K. Teshima, Y. Shirai and T. Miyasaka, *J. Am. Chem. Soc.*, 2009, **131**, 6050–6051.

2 H. S. Kim, C. R. Lee, J. H. Im, K. B. Lee, T. Moehl, A. Marchioro, S. J. Moon, R. Humphry-Baker, J. H. Yum, J. E. Moser, M. Grätzel and N. G. Park, *Sci. Rep.*, 2012, **2**, 591.

3 M. A. Green, A. Ho-Baillie and H. J. Snaith, *Nat. Photonics*, 2014, **8**, 506–514.

4 H. P. Zhou, Q. Chen, G. Li, S. Luo, T. B. Song, H. S. Duan, Z. R. Hong, J. B. You, Y. S. Liu and Y. Yang, *Science*, 2014, **345**, 542–546.

5 Z. K. Tan, R. S. Moghaddam, M. L. Lai, P. Docampo, R. Higler, F. Deschler, M. Price, A. Sadhanala, L. M. Pazos, D. Credgington, F. Hanusch, T. Bein, H. J. Snaith and R. H. Friend, *Nat. Nanotechnol.*, 2014, **9**, 687–692.

6 G. Xing, N. Mathews, S. S. Lim, N. Yantara, X. Liu, D. Sabba, M. Grätzel, S. Mhaisalkar and T. C. Sum, *Nat. Mater.*, 2014, **13**, 476–480.

7 L. Dou, Y. M. Yang, J. You, Z. Hong, W. H. Chang, G. Li and Y. Yang, *Nat. Commun.*, 2015, **5**, 5404.

8 Y. Ogomi, A. Morita, S. Tsukamoto, T. Saitho, N. Fujikawa, Q. Shen, T. Toyoda, K. Yoshino, S. S. Pandey, T. L. Ma and S. Hayase, *J. Phys. Chem. Lett.*, 2014, **5**, 1004–1011.

9 S. Kazim, M. K. Nazeeruddin, M. Grätzel and S. Ahmad, *Angew. Chem., Int. Ed.*, 2014, **53**, 2812–2824.

10 Q. Dong, Y. Fang, Y. Shao, P. Mulligan, J. Qiu, L. Cao and J. Huang, *Science*, 2015, **347**, 967–970.

11 P. Gao, M. Grätzel and M. K. Nazeeruddin, *Energy Environ. Sci.*, 2014, **7**, 2448–2463.

12 http://www.nrel.gov/ncpv/images/efficiency_chart.jpg.

13 J. H. Im, I. H. Jang, N. Pellet, M. Grätzel and N. G. Park, *Nat. Nanotechnol.*, 2014, **9**, 927–932.

14 K. Mahmood, B. S. Swain, A. R. Kirmani and A. Amassian, *J. Mater. Chem. A*, 2015, **3**, 9051–9057.

15 A. Bera, K. Wu, A. Sheikh, E. Alarousu, O. F. Mohammed and T. Wu, *J. Phys. Chem. C*, 2014, **118**, 28494–28501.

16 D. Y. Son, J. H. Im, H. S. Kim and N. G. Park, *J. Phys. Chem. C*, 2014, **118**, 16567–16573.

17 L. S. Oh, D. H. Kim, J. A. Lee, S. S. Shin, J. W. Lee, I. J. Park, M. J. Ko, N. G. Park, S. G. Pyo, K. S. Hong and J. Y. Kim, *J. Phys. Chem. C*, 2014, **118**, 22991–22994.

18 Y. Li, J. Zhu, Y. Huang, F. Liu, M. Lv, S. Chen, L. Hu, J. Tang, J. Yao and S. Dai, *RSC Adv.*, 2015, **5**, 28424–28429.

19 Y. H. Hu, *Adv. Mater.*, 2014, **26**, 2102–2104.

20 A. Mei, X. Li, L. Liu, Z. Ku, T. Liu, Y. Rong, M. Xu, M. Hu, J. Chen, Y. Yang, M. Grätzel and H. Han, *Science*, 2014, **345**, 295–298.

21 J. H. Heo, D. H. Song, H. J. Han, S. Y. Kim, J. H. Kim, D. Kim, H. W. Shin, T. K. Ahn, C. Wolf, T. W. Lee and S. H. Im, *Adv. Mater.*, 2015, **27**, 3424–3430.

22 H. H. Wang, Q. Chen, H. Zhou, L. Song, Z. S. Louis, N. D. Marco, Y. Fang, P. Sun, T. B. Song, H. Chen and Y. Yang, *J. Mater. Chem. A*, 2015, **3**, 9108–9115.

23 D. Y. Liu and T. L. Kelly, *Nat. Photonics*, 2014, **8**, 133–138.

24 W. Ke, G. Fang, Q. Liu, L. Xiong, P. Qin, H. Tao, J. Wang, H. Lei, B. Li, J. Wan, G. Yang and Y. Yan, *J. Am. Chem. Soc.*, 2015, **137**, 6730–6733.

25 H. S. Rao, B. X. Chen, W. G. Li, Y. F. Xu, H. Y. Chen, D. B. Kuang and C. Y. Su, *Adv. Funct. Mater.*, 2015, **25**, 7200–7207.

26 K. Wang, Y. Shi, Q. Dong, Y. Li, S. Wang, X. Yu, M. Wu and T. Ma, *J. Phys. Chem. Lett.*, 2015, **6**, 755–759.

27 X. D. Liu, E. Y. Jiang, Z. Q. Li and Q. G. Song, *Appl. Phys. Lett.*, 2008, **92**, 252104.

28 D. S. Bhachu, S. Sathasivam, G. Sankar, D. O. Scanlon, G. Cibin, C. J. Carmalt, I. P. Parkin, G. W. Watson, S. M. Bawaked, A. Y. Obaid, S. Al Thabaiti and S. N. Basahel, *Adv. Funct. Mater.*, 2014, **24**, 5075–5085.

29 S. Lee, J. H. Noh, H. S. Han, D. K. Yim, D. H. Kim, J. K. Lee, J. Y. Kim, H. S. Jung and K. S. Hong, *J. Phys. Chem. C*, 2009, **113**, 6878–6882.

30 X. Lü, X. Mou, J. Wu, D. Zhang, L. Zhang, F. Huang, F. Xu and S. Huang, *Adv. Funct. Mater.*, 2010, **20**, 509–515.

31 W. Chen, Y. Z. Wu, Y. F. Yue, J. L. W. J. Zhang, X. D. Yang, H. Chen, E. B. Bi, I. Ashraful, M. Grätzel and L. Y. Han, *Science*, 2015, **350**, 944–948.

32 D. H. Kim, G. S. Han, W. M. Seong, J. W. Lee, B. J. Kim, N. G. Park, K. S. Hong, S. Lee and H. S. Jung, *ChemSusChem*, 2015, **8**, 2392–2398.

33 M. Yang, R. Guo, K. Kadel, Y. Liu, K. O'Shea, R. Bone, X. Wang, J. He and W. Li, *J. Mater. Chem. A*, 2014, **2**, 19616–19622.

34 X. Yin, Y. J. Guo, Z. S. Xue, P. Xu, M. He and B. Liu, *Nano Res.*, 2015, **8**, 1997–2003.

35 J. Y. Liao, B. X. Lei, D. B. Kuang and C. Y. Su, *Energy Environ. Sci.*, 2011, **4**, 4079–4085.

36 Y. F. Wang, J. W. Li, Y. F. Hou, X. Y. Yu, C. Y. Su and D. B. Kuang, *Chem.–Eur. J.*, 2010, **16**, 8620–8625.

37 Y. F. Xu, W. Q. Wu, H. S. Rao, H. Y. Chen, D. B. Kuang and C. Y. Su, *Nano Energy*, 2015, **11**, 621–630.

38 F. Fabregat-Santiago, G. Garcia-Belmonte, J. Bisquert, P. Bogdanoff and A. Zaban, *J. Electrochem. Soc.*, 2003, **150**, E293–E298.

39 J. H. Heo, H. J. Han, D. Kim, T. K. Ahn and S. H. Im, *Energy Environ. Sci.*, 2015, **8**, 1602–1608.

40 L. Kavan, N. Tétreault, T. Moehl and M. Grätzel, *J. Phys. Chem. C*, 2014, **118**, 16408–16418.

41 J. Obrzut and K. A. Page, *Phys. Rev. B: Condens. Matter Mater. Phys.*, 2009, **80**, 195211.

42 K. Wojciechowski, S. D. Stranks, A. Abate, G. Sadoughi, A. Sadhanala, N. Kopidakis, G. Rumbles, C. Z. Li, R. H. Friend, A. K. Y. Jen and H. J. Snaith, *ACS Nano*, 2014, **8**, 12701–12709.

43 H. J. Snaith, A. Abate, J. M. Ball, G. E. Eperon, T. Leijtens, N. K. Noel, S. D. Stranks, J. T. W. Wang, K. Wojciechowski and W. Zhang, *J. Phys. Chem. Lett.*, 2014, **5**, 1511–1515.

44 J. M. Frost, K. T. Bultler, F. Brivio, C. H. Hendon, M. Van Schifgaarde and A. Walsh, *Nano Lett.*, 2014, **14**, 2584–2590.

45 E. L. Unger, E. T. Hoke, C. D. Bailie, W. H. Nguyen, A. R. Bowring, T. Heumuller, M. G. Christoforo and M. D. McGehee, *Energy Environ. Sci.*, 2014, **7**, 3690–3698.

46 D. Liu, J. Yang and T. L. Kelly, *J. Am. Chem. Soc.*, 2014, **136**, 17116–17122.

47 D. Zhong, B. Cai, X. Wang, Z. Yang, Y. Xing, S. Miao, W. H. Zhang and C. Li, *Nano Energy*, 2015, **11**, 409–418.

48 Q. Dong, Y. Shi, K. Wang, Y. Li, S. Wang, H. Zhang, Y. Xing, Y. Du, X. Bai and T. Ma, *J. Phys. Chem. C*, 2015, **119**, 10212–10217.

49 V. Gonzalez-Pedro, E. J. Juarez-Perez, W. S. Arsyad, E. M. Barea, F. Fabregat-Santiago, I. Mora-Sero and J. Bisquert, *Nano Lett.*, 2014, **14**, 888–893.

50 A. R. Pascoe, N. W. Duffy, A. D. Scully, F. Huang and Y. B. Cheng, *J. Phys. Chem. C*, 2015, **9**, 4444–4453.

51 E. J. Juarez-Perez, M. Wuβler, F. Fabregat-Santiago, K. Lakus-Wollny, E. Mankel, T. Mayer, W. Jaegermann and I. Mora-Sero, *J. Phys. Chem. Lett.*, 2014, **5**, 680–685.

52 W. Ke, G. Fang, J. Wang, P. Qin, H. Tao, H. Lei, Q. Liu, X. Dai and X. Zhao, *ACS Appl. Mater. Interfaces*, 2014, **6**, 15959–15965.

53 W. Tress, N. Marinova, O. Inganäs, M. K. Nazeeruddin, S. M. Zakeeruddin and M. Grätzel, *Adv. Energy Mater.*, 2015, **5**, 1400812.

54 S. Ryu, J. H. Noh, J. Jeon, Y. C. Kim, W. S. Yang, J. Seo and S. I. Seok, *Energy Environ. Sci.*, 2014, **7**, 2614–2618.